Metal Foreign Object Detection in ICPT System via Multi-Parameter Information Fusion: Based on Transfer Dictionary Learning

Zhan'anxin TONG, Jianhui SU, Shiyu WANG, Yan DU, and Meiqin MAO

***Abstract*—Aiming at the reliability challenge of metal foreign object detection (FOD) in inductive coupled power transfer (ICPT) systems, a fault classification strategy based on incremental transfer dual-dictionary learning is first proposed. The method first constructs a safety dictionary and a base foreign object dictionary, and introduces a reconstruction error ratio as a decision criterion to achieve fault diagnosis of metal foreign objects. Subsequently, to further enhance generalization capability, incremental transfer learning is integrated to improve the dictionary model. This involves dynamically updating the foreign object dictionary using small samples of unknown metals, with atom addition and fine-tuning to quickly adapt to new foreign object features. Finally, the trained model is evaluated. Experimental results demonstrate that the proposed method achieves a recall rate of over 95% for unfamiliar metal foreign objects after transfer, verifying the effectiveness of the detection approach. This method retains the advantages of unsupervised learning while requiring no detection coils, significantly enhancing its adaptability to complex application scenarios.**

***Index Terms*—Dictionary learning, foreign object detection, inductively coupled power transfer, reconstruction error ratio, transfer learning.**

I. Introduction

In general scenarios, the primary method for charging systems remains wired contact charging, which presents issues such as poor contact, mechanical wear, and poor environmental adaptability. Inductive coupled power transfer (ICPT) technology is widely used in charging equipment for vehicles [1] such as automated guided vehicles (AGV) [2], unmanned aerial vehicle (UAV) [3] and unmanned underwater vehicle (UUV) [4] in various industrial scenarios due to its high transmission efficiency, moderate transmission distance, and strong anti-misalignment capability [5]–[9]. This technology is safe, efficient, and features electrical isolation, enabling electrical equipment in specific environments to achieve kilowatt-level charging power within a certain air gap. However, even if the ICPT system ensures intrinsic safety, the underlying principle of electromagnetic induction can cause metallic foreign objects intruding into the charging area to consume extra energy through eddy current effects, thereby posing risks such as localized overheating, fire hazards, and reduced system efficiency [10]. Therefore, FOD is a necessary function for improving the safety and stability of ICPT systems, and it is essential to conduct research on this.

Currently, researchers have proposed various FOD detection methods, which can be divided into two main categories based on whether external detection devices are used. FOD methods without detection devices mainly include power detection method, quality factor detection method, parameter detection method, visual detection method, thermal imaging detection method, and radar detection method. The first three methods, which detect the presence of foreign objects by monitoring changes in transmission power or system parameters, are only suitable for low-power applications such as mobile phone wireless charging. In high-power wireless charging systems, where the charging area is significantly larger, these methods fail to achieve the resolution required to detect small foreign objects. For example, in a 10 kW ICPT system, the impact of an aluminum can or a set of keys on the transmission power and coil quality factor is almost imperceptible. However, the latter three detection methods undoubtedly significantly increase equipment costs and are prone to misjudgment due to environmental influences.

Although the use of detection coils for FOD increases the need for detection devices, the cost remains controllable. This approach is currently widely adopted and is primarily divided into magnetic flux detection and impedance detection methods: by comparing the changes in magnetic flux or impedance between detection coils [11], rapid and accurate detection of metal foreign objects is achieved. However, such methods have various shortcomings. For instance, to address the issue of blind zone in detection coils, an incomplete compensation detection method has been proposed [12], or various multi-layer detection coil designs have been suggested [13], [14]; to address the issue of reduced FOD accuracy caused by coil misalignment

Manuscript received November 5, 2025; revised January 13, 2026 and February 8, 2026; accepted March 31, 2026. Date of publication June 30, 2026; date of current version April 28, 2026. This work was supported by the National Key Research and Development Program of China under the grant 2021YFB2601403. (*Corresponding Author: Jianhui Su.*)

All authors are with Research Center for Photovoltaic Systems Engineering of Ministry of Education, Hefei University of Technology, Hefei 230009, China, and the School of Electrical Engineering and Automation, Hefei University of Technology, Hefei 230009, China (e-mail: tongzhan1996@mail.hfut.edu.cn; su_chen@hfut.edu.cn; shiyu99@mail.hfut.edu.cn; dydf@sina.com; mmqmail@163.com).

Digital Object Identifier 10.24295/CPSSTPEA.2026.000013

[15] proposed a voltage vector decomposition (VVD) method; [16] proposed a high-order compensation topology to amplify impedance changes and address the issue of low sensitivity at the edges of the detection area; [17] achieved the detection of different metal objects by utilizing varying detection frequencies and a unique coil design. In summary, whether measuring the system's magnetic flux or changes in impedance, diverse detection coils and backend circuit designs are indispensable, though the fundamental principles remain unchanged. Meanwhile, the more refined the detection coils and the more complex the backend circuits, the greater the need for numerous detection branches and scanning control structures. This undoubtedly significantly increases the cost of wireless charging systems.

In recent years, with the rapid development of artificial intelligence algorithms, some scholars have attempted to use neural networks and machine learning methods to achieve FOD, opening up new implementation approaches for FOD technology. The common approach is to categorize FOD as a binary classification problem of whether foreign objects are present or not. Some researchers have proposed the use of multiple detection methods, including neural networks (NN) [18], machine learning [19], support vector machines (SVM), and naive bayes classifiers [20], achieving a detection accuracy of over 80%. [21] used a multilayer feedforward neural network based on multi-valued neurons to process the phase of voltage and current at both the transmitting and receiving ends for FOD. These methods, by learning from large amounts of data, can construct complex nonlinear mapping relationships, demonstrating significant potential in distinguishing foreign object disturbances from normal operational fluctuations. Nevertheless, the performance of such detection models is highly dependent on massive, diverse, and accurately labeled training data. However, obtaining real-world experimental data that covers all types, sizes, and locations of foreign objects, as well as various working conditions, is both costly and time-consuming.

To the best of our knowledge, this work represents the first attempt to integrate dictionary learning [22], [23] with incremental transfer learning [24] for the application of FOD in wireless charging systems. Unlike existing neural network-based approaches that treat FOD as a static, black-box binary classification problem requiring massive retraining for new scenarios, a dynamic unsupervised dual-dictionary learning framework is proposed in this paper. The specific novelties and contributions are three-fold: First, a dual-dictionary architecture is constructed to mathematically decouple the sparse features of foreign objects from the dense variations of normal system operation (e.g., load shifts and misalignment), effectively solving the feature coupling issue in sensorless detection. Second, a reconstruction error ratio (RER) is introduced as a physics-interpretable decision criterion, replacing opaque probability scores with a metric that quantifies signal deviation from the safe subspace. Third, to address the poor generalization of traditional models toward unseen metals, an incremental dictionary expansion strategy is developed. This allows the system to rapidly update the foreign object dictionary using small samples (few-shot learning) without forgetting of the

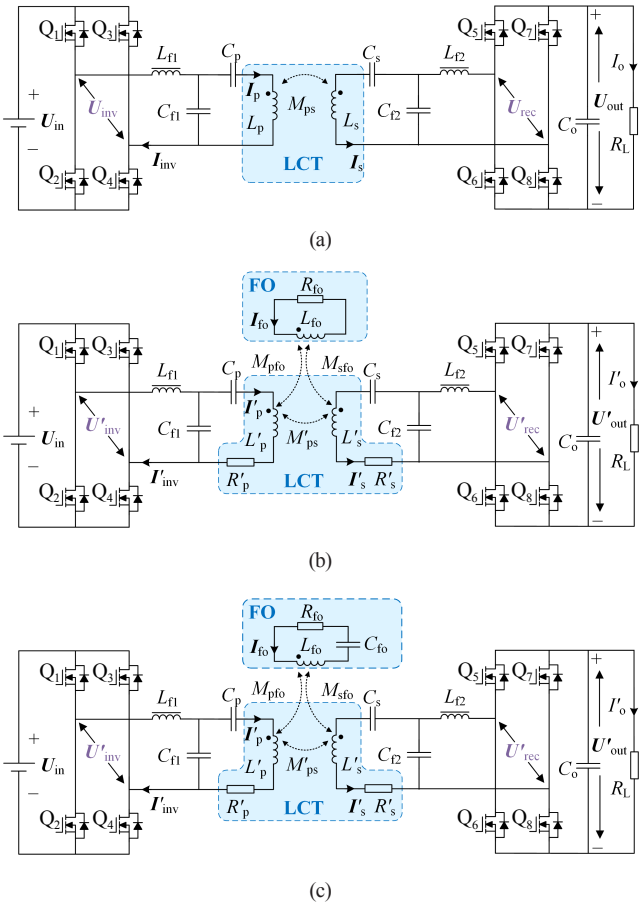

(a)

(b)

(c)

Fig. 1. Schematic diagram of ICPT system. (a) Normal state. (b) Non-ferromagnetic metals foreign object intrusion state. (c) Ferromagnetic metals foreign object intrusion state.

safety knowledge. The experimental results show that the model achieved a recall rate of over 95% for unfamiliar metal foreign objects. This method of knowledge transfer does not require extensive and complex datasets or additional auxiliary detection coils, significantly reducing both model training costs and hardware costs while meeting the detection needs for diverse metal foreign objects.

II. System Modeling

A. ICPT Equivalent Model

As shown in Fig. 1(a), the ICPT system primarily consists of two parts generally: the ground assembly (GA) and the vehicle assembly (VA). The GA section mainly includes a high frequency inverter, a compensation network, and a transmitting coil. The compensation network adopts a dual-side LCC structure to more easily maintain constant transmitter coil current and output current, it mainly includes the series inductor L_{f1} and L_{f2}, parallel capacitor C_{f1} and C_{f2}, and series capacitor C_p and C_s, the self-inductance of the transmitting coil is L_p, and the self-inductance of the receiving coil is L_s. The VA section consists of a compensation network, an active rectifier or uncontrolled diode rectifier, and an output filter. The inverter

output current on GA is i_{inv}, the output voltage is u_{inv}, and the coil current is i_p. Similarly, the rectified input voltage at the VA terminal is u_{rec}, the input current is i_{rec}, and the coil current is i_s. If the influence of parasitic parameters is not considered, the fundamental mutual inductance model of the circuit can be expressed as:

$$\begin{bmatrix} Z_1 & Z_{cf1} & 0 & 0 \\ Z_{cf1} & Z_2 & -Z_M & 0 \\ 0 & -Z_M & Z_3 & Z_{cf2} \\ 0 & 0 & Z_{cf2} & Z_4 \end{bmatrix} \begin{bmatrix} i_{inv} \\ i_p \\ i_s \\ i_{res} \end{bmatrix} = \begin{bmatrix} v_{inv} \\ 0 \\ 0 \\ -u_{res} \end{bmatrix} \tag{1}$$

where:

$$\begin{cases} Z_1 = j\omega L_{f1} + \dfrac{1}{j\omega C_{f1}} \\ Z_2 = j\omega L_p + \dfrac{1}{j\omega C_p} + \dfrac{1}{j\omega C_{f1}} \\ Z_3 = j\omega L_s + \dfrac{1}{j\omega C_s} + \dfrac{1}{j\omega C_{f2}} \\ Z_4 = j\omega L_{f2} + \dfrac{1}{j\omega C_{f2}} \\ Z_{cf1} = \dfrac{1}{j\omega C_{f1}} \\ Z_{cf2} = \dfrac{1}{j\omega C_{f2}} \\ Z_M = j\omega M_{ps} \end{cases} \tag{2}$$

Under ideal resonant conditions, the system operating frequency and compensation components satisfy:

$$Z_1 = Z_2 = Z_3 = Z_4 \tag{3}$$

At this point, the system achieves zero-phase-angle (ZPA), but under these conditions, the inverter struggles to achieve zero-voltage-switching (ZVS) due to dead-time control. Typically, the series compensation inductor is slightly increased to make the output impedance slightly inductive.

After the intrusion of a metallic foreign object, the electromagnetic field inside the ICPT system induces eddy currents within the metal. These eddy currents flow in closed loops along the interior of the metal. For non-ferromagnetic metals, the closed eddy current field can be equivalently modeled as a short-circuit loop consisting of a resistor and an inductor in series, forming a three-coil, three-port coupling model with the loosely coupled transfer (LCT) mechanism, as illustrated in the Fig. 1(b), the changes in inductance and resistance components can be analyzed:

$$R_p^{'} = R_p + \frac{\omega^2 M_{pfo}^2}{R_{fo}^2 + (\omega L_{fo})^2} R_{fo} \tag{4}$$

$$R_s^{'} = R_p + \frac{\omega^2 M_{sfo}^2}{R_{fo}^2 + (\omega L_{fo})^2} R_{fo} \tag{5}$$

$$L_p^{'} = L_p - \frac{\omega^2 M_{pfo}^2}{R_{fo}^2 + (\omega L_{fo})^2} L_{fo} \tag{6}$$

$$L_s^{'} = L_s - \frac{\omega^2 M_{sfo}^2}{R_{fo}^2 + (\omega L_{fo})^2} L_{fo} \tag{7}$$

$$M_{ps}^{'} = M_{ps} - \frac{j\omega M_{pfo} M_{sfo}}{R_{fo} + j\omega L_{fo}} \tag{8}$$

The third port of the LCT mechanism forms a short-circuit loop due to the eddy current field, and all parameters of the LCT mechanism will change under the influence of metal foreign objects. Among them, $R_p^{'}$ and $R_s^{'}$ are the equivalent resistances of the transmitting coil and receiving coil after metal intrusion, $L_p^{'}$ and $L_s^{'}$ are the equivalent self-inductances of the transmitting coil and receiving coil after metal intrusion, $M_{ps}^{'}$ is the mutual inductance between the transmitting coil and receiving coil after metal intrusion, L_{fo} is the equivalent inductance of the metal foreign object, M_{pfo} is the mutual inductance between the transmitting coil and the metal foreign object, and M_{sfo} is the mutual inductance between the receiving coil and the metal foreign object. Affected by electromagnetic parameters, the current of the transmitting coil changes to $I_p^{'}$, the current of the receiving coil changes to $I_s^{'}$, the inverter output current at the GA terminal changes to $I_{inv}^{'}$, and the rectifier input current at the VA terminal changes to $I_{rec}^{'}$.

It can be seen that non-ferromagnetic metal foreign objects can affect the parameters of the LCT mechanism. The underlying principle of their intrusion mechanism is well understood, specifically manifesting in the resistance and inductance of the transmission coil. According to the analysis in [17], non-ferromagnetic metals can increase resistance and decrease equivalent inductance; whereas ferromagnetic metals differ from non-ferromagnetic ones: while generating eddy current effects that suppress the magnetic field, they also exhibit a magnetic effect that enhances the field. This magnetic effect leads to an increase in equivalent self-inductance, which can be equivalently represented as a series connection of C_{fo} and L_{fo}. Not only does this increase resistance and reduce equivalent inductance, but it also mitigates the extent of the inductance reduction. Both effects directly manifest as a decline in the coil's Q value. The impact of ferromagnetism on electromagnetic parameters is specifically reflected as:

$$R_p^{'} = R_p + \frac{\omega^2 M_{pfo}^2}{R_{fo}^2 + \left(\omega L_{fo} - \dfrac{1}{\omega C_{fo}}\right)^2} R_{fo} \tag{9}$$

$$R_s^{'} = R_p + \frac{\omega^2 M_{sfo}^2}{R_{fo}^2 + \left(\omega L_{fo} - \dfrac{1}{\omega C_{fo}}\right)^2} R_{fo} \tag{10}$$

$$L_p^{'} = L_p - \frac{\omega^2 M_{pfo}^2}{R_{fo}^2 + \left(\omega L_{fo} - \dfrac{1}{\omega C_{fo}}\right)^2} \left(L_{fo} - \frac{1}{\omega^2 C_{fo}}\right) \tag{11}$$

$$L_s^{'} = L_s - \frac{\omega^2 M_{sfo}^2}{R_{fo}^2 + \left(\omega L_{fo} - \dfrac{1}{\omega C_{fo}}\right)^2} \left(L_{fo} - \frac{1}{\omega^2 C_{fo}}\right) \tag{12}$$

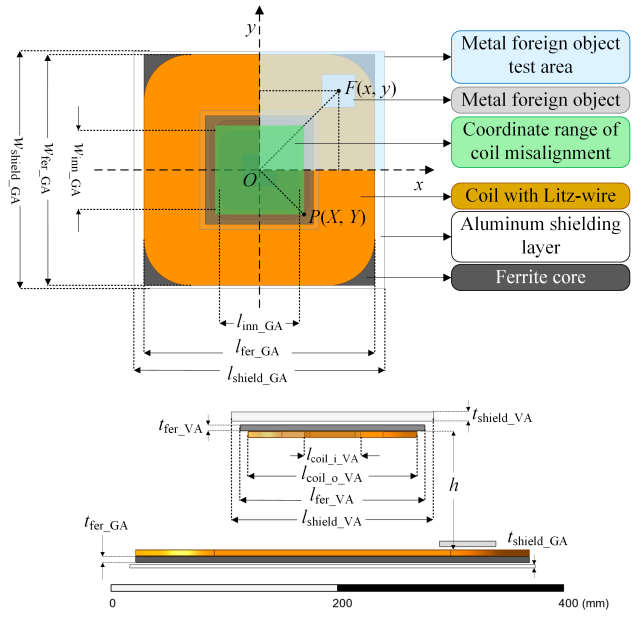

Fig. 2. LCT model with a metal foreign object.

$$M'_{ps} = M_{ps} - \frac{j\omega M_{pfo} M_{sfo}}{R_{fo} + j\omega L_{fo} + \dfrac{1}{j\omega C_{fo}}} \tag{13}$$

B. Parametric Modeling of LCT Mechanism Containing Metallic Foreign Objects

As shown in the Fig. 2, the LCT mechanism consists of a transmitting end and a receiving end. Both ends include an aluminum shielding layer, laminated PC95 ferrite cores, and planar spiral rounded rectangular Litz-wires. It is also assumed that a metal foreign object is placed on the surface of the transmitting end.

The modeling of the LCT was completed in ANSYS Electronic Desktop (Maxwell). A three-dimensional Cartesian coordinate system was established with the center O of the transmitter coil as the origin. The center of the metal foreign object is located at $F(x, y)$ on the xOy plane. Without considering the angular deflection at the receiver end and only accounting for planar offset, the position of the VA-side LCT can be expressed as $P(X, Y, h)$. TABLE I summarizes the geometric parameters of the LCT mechanism.

TABLE I
PARAMETERS FOR LCT MODEL

Symbol	Quantity	Value/mm
l_{inn_GA}	Coil inner ring length (GA)	120
w_{inn_GA}	Coil inner ring width (GA)	120
l_{fer_GA}	Ferrite core length (GA)	360
w_{fer_GA}	Ferrite core width (GA)	360
l_{shield_GA}	Shield length (GA)	380
w_{shield_GA}	Shield width (GA)	380
$l_{coil\_i\_VA}$	Coil inner ring length (VA)	50
$l_{coil\_o\_VA}$	Coil inner ring width (VA)	150
l_{fer_VA}	Ferrite core length (VA)	160
l_{shield_VA}	Shield length (VA)	180
t_{shield_VA}	Shield thickness (VA)	8
t_{fer_VA}	Ferrite core thickness (VA)	5
t_{fer_GA}	Ferrite core thickness (GA)	5
t_{shield_GA}	Shield thickness (GA)	3
h	Vertical transmission distance	100~150
X	Lateral offset (VA)	0 ~ ±75
Y	Longitudinal offset (VA)	0 ~ ±75
x	Lateral coordinates of metal FO	0 ~ 190
y	Longitudinal coordinates of metal FO	0 ~ 190

III. ALGORITHM DESIGN

A. Dictionary Learning

The factors affecting system parameters are multifaceted. Considering variations in coil offset, transmission distance, foreign object position, material, size, operating frequency, and output load, constructing a dataset that consists all these changing conditions would undoubtedly be massive, significantly increasing the training costs of machine learning. Dictionary learning, through the method of sparse coding representation, forms an efficient feature extraction mechanism that can significantly reduce the workload of training. Classifiers trained based on sparse coding can effectively perform the task of FOD.

Metal FO can alter the electromagnetic parameters of the system, thereby affecting electrical performance. Extracting the electrical characteristic data of the system forms a feature vector. Assuming there are n feature dimensions and m sample instances, the feature matrix composed of all original samples is:

$$Y = [y_1, y_2, \ldots, y_k] \in \mathbb{R}^{n \times m} \tag{14}$$

The essence of dictionary learning is the sparse representation of data through dimensionality reduction. Its core idea is that any signal can be approximately represented as a linear combination of a small number of atoms from an overcomplete dictionary. The goal of dictionary learning is to learn a dictionary from Y:

$$D = [d_1, d_2, \ldots, d_k] \in \mathbb{R}^{n \times k} \tag{15}$$

and sparse coding matrix:

$$A = [\alpha_1, \alpha_2, \ldots, \alpha_m] \in \mathbb{R}^{k \times m} \tag{16}$$

so that each sample can be sparsely represented as:

$$Y \approx DA \tag{17}$$

Each column of D is a basis vector, and each column α_i of A represents the sparse representation of the sample y_i under the

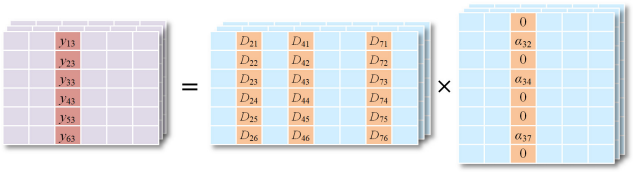

Fig. 3. Sparse representation principle of dictionary learning.

dictionary. As shown in Fig. 3, if the sparsity is 3, then A can have at most 3 non-zero entries, corresponding to 3 atoms in the dictionary.

The optimization problem for dictionary learning can be expressed as minimizing the reconstruction error:

$$\langle D, A\rangle = \arg\min \|Y - DA\|_F^2; \text{ s.t.} \|\alpha_i\|_0 \leqslant T, i = 1,2,\ldots,N \quad (18)$$

where $\|\alpha_i\|_0$ denotes the L_0 norm of the vector α_i, is the number of all non-zero elements in the vector, and T represents the sparsity. In practical applications, to reduce computational complexity, we often turn to minimizing the convex relaxation L_1 norm of the L_0 norm, which still ensures the sparsity of the sparse matrix. At this point, the equation becomes:

$$\langle D, A\rangle = \arg\min \|Y - DA\|_F^2; \text{ s.t.} \|\alpha_i\|_1 \leqslant T, i = 1,2,\ldots,N \quad (19)$$

As the core step of dictionary learning, sparse coding aims to linearly combine atoms in the dictionary while ensuring maximum sparsity, where the degree of sparsity directly reflects data compression. The sparse coding problem can be formulated as:

$$\min_{\alpha} \|y - D\alpha\|; \text{ s.t.} \|\alpha\|_1 \leqslant T \quad (20)$$

Orthogonal matching pursuit (OMP), as an improved greedy algorithm, can be used to solve the above equation and obtain the currently optimal sparse matrix A. After obtaining the sparse representation, with the sparse coefficients fixed, dictionary updating can be performed using the K-singular value decomposition (K-SVD) method or joint optimization based on coordinate descent (CD).

B. Incremental Dictionary Transfer Learning

Dictionary learning, as a feature extraction method, has been widely applied within the framework of transfer learning. However, the influence of different metallic foreign objects on system parameters exhibits material specificity, and existing datasets cannot cover all types of metals. As a result, the trained foreign object dictionaries have certain limitations when encountering unfamiliar metals. Therefore, based on the presence or absence of metallic foreign objects, the system can be categorized into safe and foreign object states. Fig. 4 is the overall flowchart of the model training process, which is generally divided into two stages: data preprocessing and training. During data processing, the dataset needs to be first divided into a safe-state sample set and a foreign-object-state sample set. Based on the feature data from these two states, the normal dictionary D_{safe} representing the safe state of the system and the foreign-object dictionary D_{metal} representing the abnormal

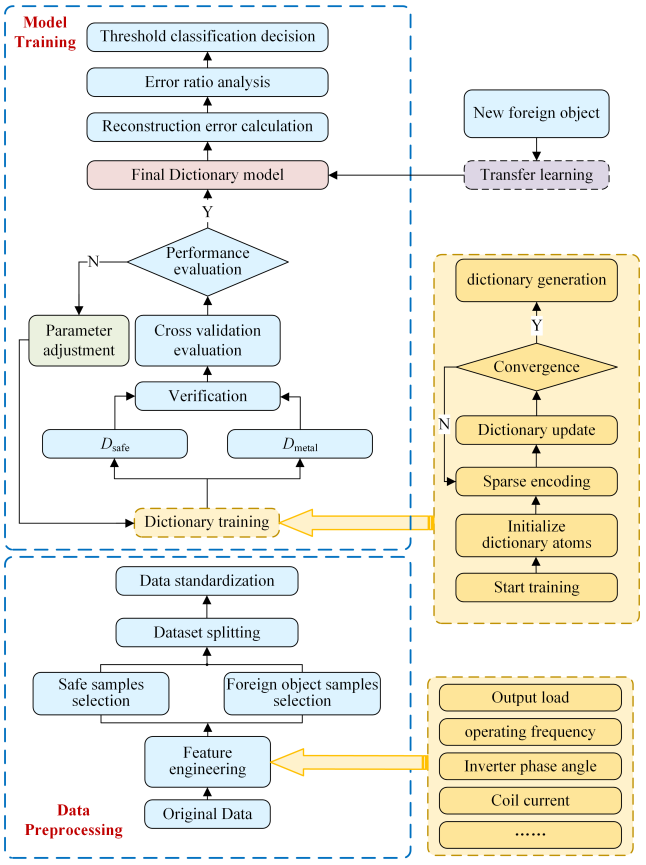

Fig. 4. Double dictionary construction and model training flowchart.

(foreign object) state of the system can be trained separately. The collaborative work of dual dictionaries can effectively enhance the accuracy and robustness of foreign object detection. However, dictionary learning itself has certain limitations. Each dictionary is trained based on its own sample data and is essentially a feature representation derived from the training data, which has limited generalization ability for unseen patterns. The system can only effectively detect metal types that were known during training. If metal types not present during training (with different materials, sizes, or shapes) appear, the system may fail to detect them accurately. Recollecting samples of all metal types is costly and not practical in real-world scenarios.

Transfer learning (TL) enables the application of knowledge learned from one domain (the source domain) to another related but different domain (the target domain). To address the issue of effectively identifying unfamiliar metallic foreign objects when they intrude into a system, a pre-trained dual-dictionary model is used to perform sparse representation of the system parameters after the intrusion. By incrementally updating D_{metal} with only a small number of samples from the target domain, rapid detection of unknown metallic objects can be achieved.

The framework diagram of the transfer learning part in the system is shown in Fig. 5. In this system, the source domain refers to the training model with known metal types, while the target domain corresponds to the model for unfamiliar metal

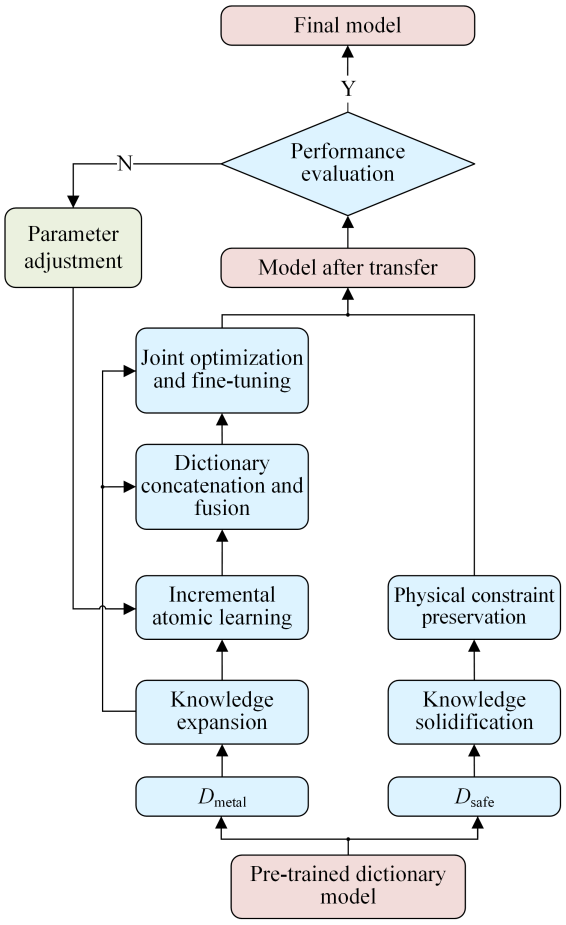

Fig. 5. Transfer learning algorithm framework based on incremental dictionary updates.

types. The system adopts an incremental dictionary learning update strategy which is an innovative unsupervised transfer method that does not require specific metal type labels. By preserving the invariance of safety state knowledge, it expands the foreign object dictionary D_{metal} through incremental learning to meet the detection needs of new metal types.

The mathematical theory of transfer learning is built upon the dual constraints of knowledge transfer and preservation. Let the original model parameters be θ_0, the new domain data be D_{target}, and the goal is to learn new parameters θ^* such that:

$$\theta^* = \arg\min_{\{\theta\}} [l(D_{target}, \theta) + \lambda_1 R(\theta) + \lambda_2 \|\theta - \theta_0\|_2^2] \quad (21)$$

where $l(D_{target}, \theta)$ is the loss function on the new data, $R(\theta)$ is the regularization term, $\|\theta - \theta_0\|_2^2$ is the knowledge preservation constraint term, and λ_1 and λ_2 are the balancing parameters. In this system, the security dictionary D_{safe} remains entirely unchanged to ensure the continuity of system security knowledge, while D_{metal} is expanded through incremental atomic learning to accommodate the detection needs of unfamiliar metallic foreign objects.

C. Decision-Making Mechanism

After obtaining the sparse coding of the dual dictionaries via OMP, the corresponding reconstruction errors can be derived, as shown in the equation. This study proposes using the RER from the safe dictionary to that from the foreign object dictionary as a key decision feature. Physically, this ratio reflects the degree of deviation of the tested sample from the normal operating mode. A offline optimal threshold optimization method is employed to minimize the false alarm rate while ensuring a 95% recall rate. Ultimately, by comparing the reconstruction error ratio with the optimal threshold, a binary classification decision between "safe" and "foreign object" is achieved. The optimal threshold θ_{opt} is determined via a statistical traversal method on the validation set. Let $P(\theta)$ and $R(\theta)$ be the precision and recall at a given threshold θ. The selection objective is defined to maximize the classification performance while strictly satisfying the safety requirement:

$$\theta_{opt} = \arg\max_{\theta} \left(\frac{2 \cdot P(\theta) \cdot R(\theta)}{P(\theta) + R(\theta)} \right) \text{s.t. } R(\theta) \geqslant 0.95 \quad (22)$$

By sweeping θ across the distribution of RER values, the optimal separation point is identified. Since RER is a relative ratio metric, this threshold exhibits high robustness against power level fluctuations and does not require real-time retuning.

Let ε_{safe} and ε_{metal} be the normalized secure dictionary reconstruction errors, respectively:

$$\begin{cases} \varepsilon_{safe} = \dfrac{\|y - D_{safe}\alpha_{safe}\|_2}{\|y\|_2} \\ \varepsilon_{metal} = \dfrac{\|y - D_{metal}\alpha_{metal}\|_2}{\|y\|_2} \end{cases} \quad (23)$$

then:

$$\text{RER}(y) = \frac{\varepsilon_{safe}}{\varepsilon_{metal}} \quad (24)$$

If the optimal threshold is θ_{opt}, then the decision rule is:

$$\text{Decision} = \begin{cases} \text{Safety State} & \text{RER} < \theta_{opt} \\ \text{FO State} & \text{RER} > \theta_{opt} \end{cases} \quad (25)$$

This decision rule transforms the complex pattern recognition problem into an intuitive ratio comparison. When the RER is below the threshold, it indicates that the sample more closely matches the safe dictionary; conversely, it suggests a closer match to an abnormal state.

IV. Dataset and Evaluation Indicators

A. Dataset Establishment and Preprocessing

Build a stable and representative dataset to support the offline training and validation of the model. By leveraging neural networks and machine learning to capture the complex nonlinear relationships among system variables, the classification performance of the model can be improved.

First, by conducting parametric simulations with metal foreign objects of different sizes and materials under various $F(x, y)$

TABLE II
CONFUSION MATRIX

Actual result	Prediction result of model	
	Safety	Danger
Safety	TP	FN
Danger	FP	TN

parameters, as well as with the LCT structure at the receiving end under different $P(X, Y, h)$ coordinates, a series of inductance and resistance matrix datasets can be obtained. However, acquiring all LCT parameters for every combination of positions would lead to a drastic increase in data volume. For example, if there are 3 types of distinct foreign objects, and data is collected at 1mm intervals for both coil offset and foreign object position, the total number of data points in the entire dataset would reach 3.375×10^9, which is clearly unacceptable.

Next, to reduce the data volume, the method of random sampling within the range of each varying parameter was adopted. By writing MATLAB parametric simulation code, the inductance and resistance matrix set results output by ANSYS Maxwell were imported into the Simulink model, and a three-coil coupled inductance system was constructed. Under automated parameter simulation conditions, the electrical parameter characteristic quantities of the ICPT system under different foreign object scenarios were obtained, forming the final dataset.

Finally, our dataset contains a total of 9,071 samples, including 3,296 samples of normal system states without foreign objects and 5,775 samples of abnormal system states with foreign objects present.

Set the parameters of the circuit simulation model in MATLAB. According to the TABLE I, datasets accounting for variations in coil offset, transmission distance, foreign object position, and material parameters were imported into the circuit model. Within the frequency range of 80–90 kHz, the load variation range was set to 10–100 Ω, and the input bus voltage variation range was adjusted to 400–800 V. This setup aimed to simulate multiple scenarios of foreign object intrusion into the system as well as normal operation without foreign objects. Three distinct types of metal foreign objects were used in this study: an iron sheet, an aluminum can, and a bunch of keys. Similarly, all varying parameters were randomly sampled within their respective ranges.

To enrich the dataset as comprehensively as possible, a total of 11 feature parameters were collected, specifically: switching frequency (f), load (R_L), inverter output phase difference (φ_i), average current of the transmitter coil ($I_{coil\_RMS,i}$), average voltage of the compensation inductor ($V_{Lf1\_RMS,i}$), voltage of the parallel compensation capacitor ($V_{Cf1\_RMS,i}$), voltage of the series compensation capacitor ($V_{Cp\_RMS,i}$), input bus voltage ($V_{bus,i}$), input bus current ($I_{bus,i}$), output current of the receiver ($I_{output,i}$), and output voltage ($V_{output,i}$), where i is the sample number.

Additionally, to further explore the relationship between feature variations and foreign object intrusion, three additional features were introduced in the feature engineering process, namely: phase offset, the capacitor voltage ratio of the LCC compensation network, and load normalization. The expressions for these three feature values are as follows:

$$\begin{cases} \Delta\varphi_i = \varphi_i - \dfrac{1}{N_{RL}}\sum_j \varphi_i \\ R_{cap} = \dfrac{V_{Cf1\_RMS,i}}{V_{Cp\_RMS,i}} \\ I_{bus\_norm} = \dfrac{I_{bus,i}}{\sqrt{R_{L,i}}} \end{cases} \tag{26}$$

where φ_i represents the phase difference of the inverter output for the current sample; N_{RL} denotes the number of samples under the same load; $\Delta\varphi_i$ is the phase offset of the current sample relative to other samples under the same load; and j is the number of samples corresponding to the same load for the current sample; by calculating the mean phase difference of each sample relative to other samples under the same load, the normal influence of load variations on phase differences is eliminated, thereby extracting abnormal phase changes and highlighting those caused by non-load factors; R_{cap} represents the ratio of capacitor voltages in the transmitter compensation network, metal foreign objects can alter the mutual inductance and coupling coefficient, thereby changing the resonant state of the resonant cavity and causing variations in this voltage ratio, which can serve as an auxiliary feature for capturing foreign object information; I_{bus_norm} is the normalized value of the DC bus current, by normalizing the load, load-independent current anomalies are extracted, and $R_{L,i}$ denotes the sampled load value in the equation.

In model training, the dataset is first split into a training set and a test set in an 80:20 ratio. On the training set, the OMP and CD algorithms are employed to obtain sparse codes and dual dictionaries, after which the classification performance is evaluated on the test set.

B. Evaluation Indicators

Metal foreign object detection is a typical imbalanced classification problem, where the importance of accurately detecting foreign object intrusion is evidently higher than that of misjudging stable samples. Using a single accuracy metric as the model evaluation indicator is clearly insufficient to comprehensively assess model performance. Supplementary evaluations should also be conducted using recall (Recall), precision (Precision), false alarm rate (FAR), and F1 score (F1) based on the confusion matrix. The confusion matrix used to evaluate the model's classification accuracy is shown in TABLE II.

Among them, accuracy refers to the proportion of all correctly predicted samples to the total number of samples, providing a macroscopic view of the model's overall performance; Recall represents the proportion of samples that are actually foreign objects being correctly detected by the model, where a high recall rate implies a low false negative rate and serves as the most critical performance indicator; Precision indicates the proportion of samples predicted as foreign objects by the mod-

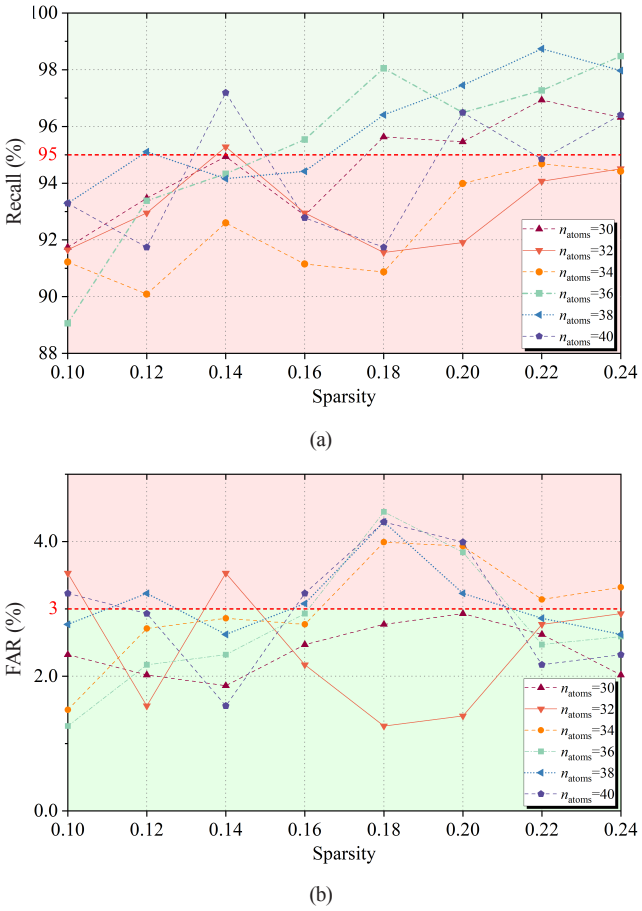

(a)

(b)

Fig. 6. Point line graph of the influence of sparsity and atomic number on the model. (a) The impact on Recall rate. (b) The impact on FAR.

el that are indeed actually foreign objects; FAR refers to the proportion of actually safe samples being misclassified as containing foreign objects; the F1 score is the harmonic mean of precision and recall, used to balance the two. Specific formula is as follows:

$$\text{Accuracy} = \frac{\text{TP} + \text{TN}}{\text{TP} + \text{TN} + \text{FP} + \text{FN}} \tag{27}$$

$$\text{Recall} = \frac{\text{TP}}{\text{TP} + \text{FN}} \tag{28}$$

$$\text{Precision} = \frac{\text{TP}}{\text{TP} + \text{FP}} \tag{29}$$

$$\text{FAR} = \frac{\text{FP}}{\text{TN} + \text{FP}} \tag{30}$$

$$\text{F1} = 2 \times \frac{\text{Precision} \times \text{Recall}}{\text{Precision} + \text{Recall}} \tag{31}$$

V. Experimental Verification

A. Hyperparameter Optimization

In dictionary learning, the number of atoms (n_{atoms}) and sparsity (S) are the two most critical parameters. n_{atoms} refers to the quantity of basis functions in the dictionary used to represent

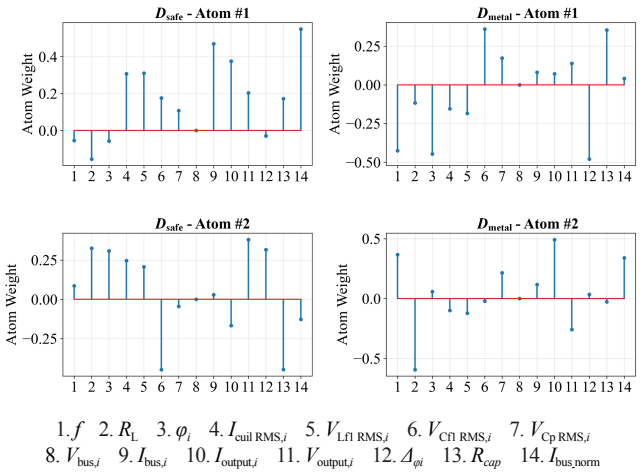

Fig. 7. Visual comparison of feature weight distributions for typed dictionary atoms.

signals. Each atom can be understood as a specific feature pattern within the signal. If n_{atoms} is too small, it may fail to capture sufficient feature patterns, leading to excessively high reconstruction errors. Conversely, an overly large number of atoms may cause model overfitting, which increases computational complexity and reduces generalization capability.

The sparsity parameter S controls the number of non-zero parameters in sparse coding. A larger sparsity parameter results in fewer non-zero entries in the encoding, which may lead to higher reconstruction errors and weaker feature representation capability. Conversely, weaker sparsity leads to lower reconstruction errors but causes feature redundancy and model overfitting.

Reasonable parameter tuning can achieve a balance between performance and computational cost. In the experiments, based on the training results of dictionary learning, we set n_{atoms} to range between 30 and 40, and the sparsity between 0.1 and 0.24. The training results are shown in the Fig. 6. Among them, Fig. 6(a) shows the relationship between Recall and sparsity for different n_{atoms}, while Fig. 6(b) illustrates the relationship between FAR and sparsity for different n_{atoms}.

When performing classification tasks, we need to consider not only detection accuracy but also ensuring that the safety false alarm rate remains at a low level. The threshold values of the metrics for the selected parameters are set to ensure a Recall rate above 95% and FAR below 3%. Comprehensive analysis of Fig. 6(a) and Fig. 6(b) reveals a critical performance optimization window. When sparsity is less than 0.16, the model exhibits lower recall due to insufficient representational capability, while the FAR remains around 3%. In the sparsity range of 0.16–0.20, the overall Recall increases, but the FAR also remains relatively high. When sparsity exceeds 0.20, although FAR drops back to a lower level, Recall generally declines as well. Considering the phenomenon where the FAR first increases and then decreases, the optimal operating interval for the model should be determined to be sparsity of 0.16–0.22. Within this interval, a certain degree of FAR is traded off to achieve higher Recall, while meeting system

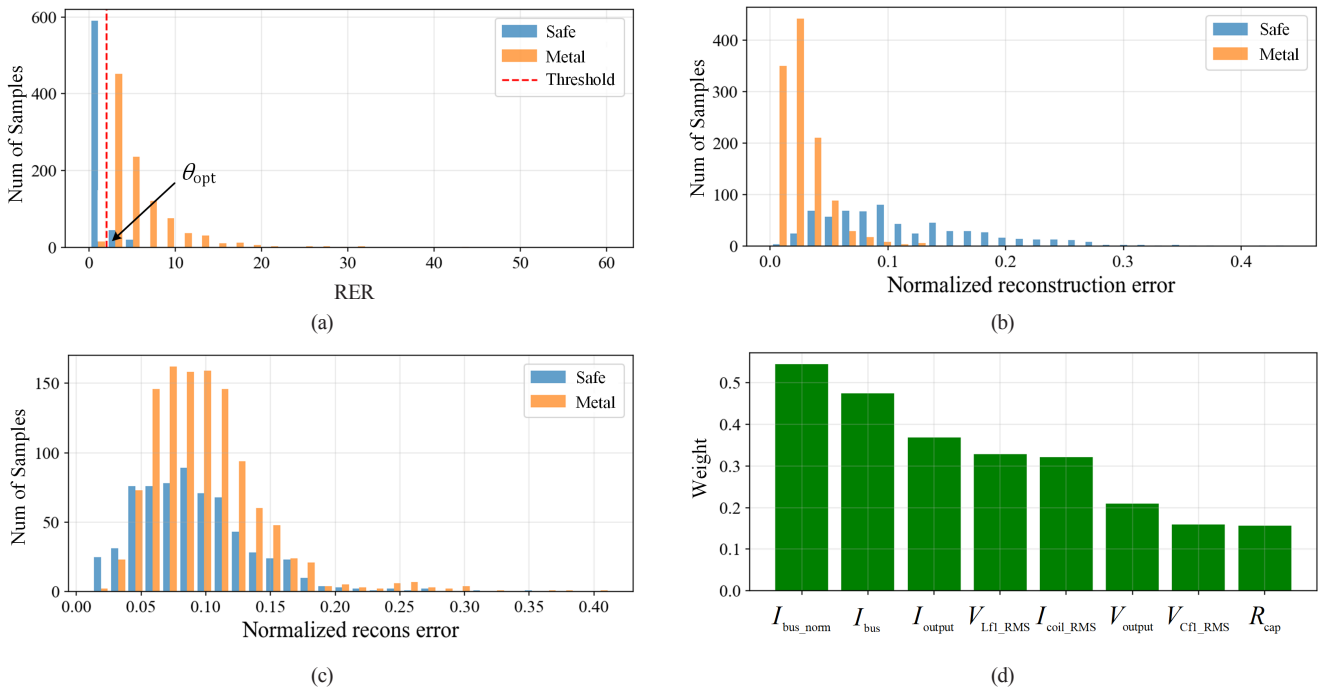

Fig. 8. Experimental results and performance validation of dictionary learning. (a) Distribution of reconstruction error ratio. (b) Distribution of reconstruction errors in foreign object dictionary. (c) Distribution of reconstruction errors in safe dictionary. (d) Importance ranking of atomic feature distribution.

safety requirements. Additionally, when n_{atoms} exceeds 38, performance improvements tend to saturate and fluctuate significantly. Comprehensively considering model complexity and performance, $n_{atoms} = 36$ and $S = 0.22$ are selected as the final model parameters. At this setting, the Recall is high, and the FAR remains within the expected range.

B. Dictionary Training Performance Validation

Dictionary learning, through iterative training, can automatically analyze the correlation weights of each feature dimension with respect to the system state. Visual analysis conducted by selecting the first two atoms from dual dictionaries provides key evidence for verifying both the algorithm's effectiveness and its physical rationality. As shown in the Fig. 7, the left column presents the visualization results of D_{safe} atoms, while the right column shows those of D_{metal} atoms. The results in the left column indicate that its atom vectors exhibit high sparsity and concentration in the 14-dimensional feature space. For example, the activation values of Atom #1 are only concentrated on a few feature dimensions with relatively smooth activation magnitudes. This sparse structure suggests that during the safe and stable operation of the ICPT system, its state is composed of a linear combination of only a few core operating parameters (e.g., coil current, resonant capacitor voltage, phase difference). In contrast, the D_{metal} atoms in the right column show a sharp contrast: they demonstrate more extensive activation distributions and several stronger activation magnitudes. The non-zero weights of the foreign object atoms are distributed across more feature dimensions, leading to a series of complex nonlinear variations.

Fig. 8 presents the experimental results and performance validation of dictionary learning. According to (24), Fig. 8(a) displays the distribution results of the RER. During reconstruction, the RER of safe samples is mostly concentrated on the left side of the threshold, indicating that safe samples are reconstructed accurately using D_{safe}, whereas reconstruction using D_{metal} is relatively poor. In contrast, for foreign object samples, their RER during reconstruction is mostly distributed on the right side of the threshold, with a high degree of separation in their distribution. Fig. 8(b) and Fig. 8(c) respectively illustrate the distribution of reconstruction errors under the foreign object dictionary and the safe dictionary. In D_{metal}, the RER of foreign object samples is significantly higher than that of safe samples; conversely, in D_{safe}, the RER of safe samples is notably lower than that of foreign object samples. This effectively demonstrates the validity of dictionary learning. Fig. 8(d) selects the feature weight distribution of the most important atom in the dictionary. It can be observed that normalized DC bus current and bus current have extremely high weights in the enhanced feature engineering. Metal foreign objects primarily affect the resonant characteristics of the power transmission link and compensation network, which fully aligns with theoretical expectations—specifically, foreign objects absorb energy through the eddy current effect, thereby altering the system's load characteristics and resonant frequency point.

C. Transfer Learning and Overall Performance

The trained foreign object dictionary triggers incremental atomic learning and dictionary concatenation fusion through transfer learning when encountering unfamiliar metals, thereby updating the foreign object dictionary and further consolidating the overall model performance of dictionary learning. As

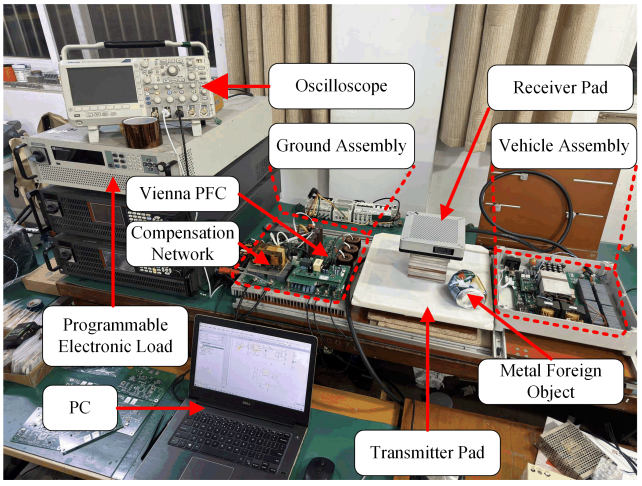

(a)

(b)

Fig. 9. Experimental platform and metal foreign objects. (a) Experimental prototype platform. (b) Metal foreign objects used for testing.

shown in Fig. 9(b), the original dataset included two types of metallic foreign objects in the experiments: nonferromagnetic soda can and ferromagnetic steel sheet. The small-sample foreign objects used as supplementary data for transfer learning were a set of keys (Transfer #1) and a broken smartwatch (Transfer #2).

The metal objects selected for testing are chosen based on common debris found in EV charging scenarios (SAE J2954). While coil-based methods often test coins, this study focuses on sensorless detection in high-power systems, where 'watch' represent a challenging small-scale object that induces complex signal distortions significantly harder to detect than in low-power applications.

To complete this experiment, we designed and built a 6.6 kW ICPT experimental prototype as shown in the Fig. 9(a). The experimental platform utilizes the TI C2000 series DSP main control chip TMS320F280039C, with the trained dictionary model deployed into the system. The system output is connected to a programmable electronic load to simulate the battery charging process. The system operating frequency is set to 85 kHz, with the system status checked and RER recorded every 5 seconds.

Benchmark tests based on the TMS320F280039C microcontroller (120 MHz) show that the complete detection process requires only about 10–20 ms per cycle. Given that the thermal time constant of metal foreign objects is on the order of tens of seconds, executing this detection algorithm in the CLA module

TABLE III
RESULT OF CONFUSION MATRIX

Index	Before Transfer (Original model)	After Transfer#1 (Updated model)	After Transfer#2 (Updated model)
Accuracy	97.30	97.57	97.51
Recall	98.70	98.84	98.81
Precision	79.34	81.05	80.65
FAR	2.86	2.57	2.63
F1	87.98	89.05	88.78

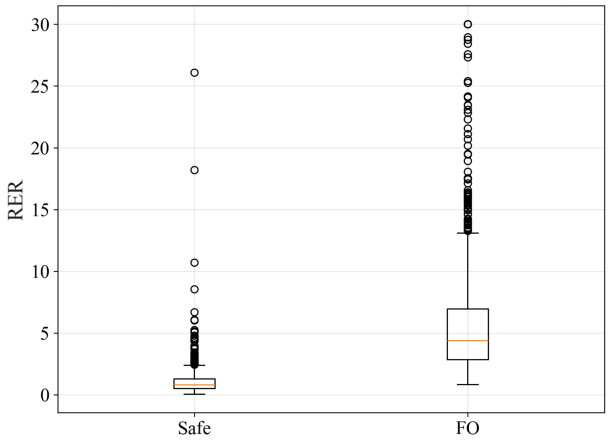

(a)

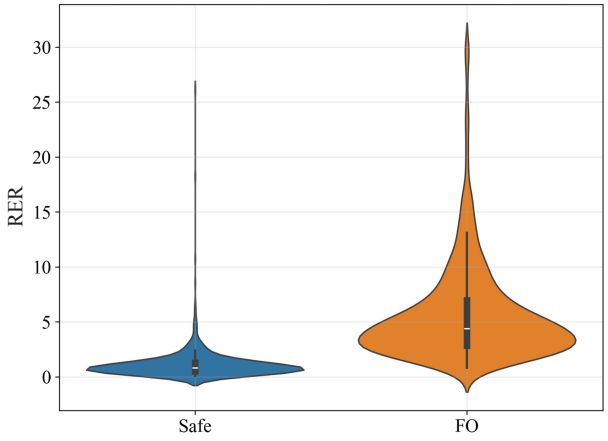

(b)

Fig. 10. Diagram of model performance. (a) Box diagram of RER. (b) Violin chart of RER.

with a 500 ms cycle not only achieves rapid and safe responses but also occupies less than 10% of the processor's resources, fully demonstrating the outstanding practicality of the real-time protection function.

First, under safe conditions, the system operates for one hour. The position of the VA-side coil is randomly adjusted within the range specified in TABLE I, and the FAR of the system is recorded to verify its stability. Next, metal foreign objects pre-trained in the dictionary model are sequentially placed at any position within the test area on the surface of the transmitter coil shown in Fig. 2. Each position is operated

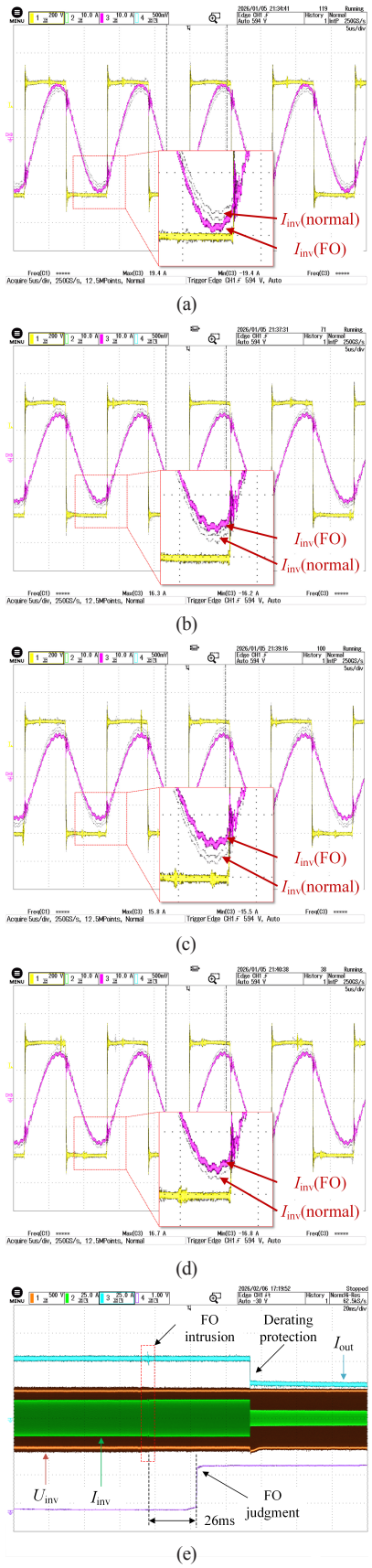

Fig. 11. Waveforms of the inverter before and after the intrusion of four different metal foreign objects. (a) Can. (b) Steel sheet. (c) Keys. (d) Smart watch. (e) System response after FO intrusion.

for two hours, with 50 random positions tested for both iron blocks and aluminum cans, covering the center, intermediate, and edge regions to verify that the RER metric remains effective regardless of the magnetic field distribution at the specific foreign object location. RER data is statistically analyzed, and the recall rate is calculated.

The comparison of model performance before and after transfer learning is presented in TABLE III. Owing to the incremental algorithm of transfer learning, which enriches the dataset to a certain degree, the system further reduces the false positive rate while maintaining a high recall rate. The results demonstrate that transfer learning effectively addresses the issue of insufficient generalization capability in dictionary learning. Specifically, by incorporating new atoms through an incremental dictionary update strategy, the representation capacity of the foreign object dictionary is enhanced. This successfully integrates domain-adaptive knowledge into the detection model, enabling the system to better identify foreign object types unseen during the training phase.

The overall performance of the model after transfer learning is shown in the Fig. 10, where Fig. 10(a) presents a box plot of the RER, and Fig. 10(b) shows its violin plot. Based on the comparative analysis of the two, the RER distributions under the system's safe state (Safe) and foreign object state (FO) exhibit significant differences, revealing the overall characteristics of the system's performance. In Fig. 10(a), the RER of the safe state is concentrated in a lower interval, with a compact box and a narrow interquartile range, and almost no outliers, indicating that the system demonstrates high stability and reliability under normal operating conditions. In contrast, the RER of the abnormal state has a relatively high median, a significantly expanded box range, and a large number of high-value outliers, reflecting intense error fluctuations under fault conditions. Fig. 10(b) further confirms this trend: the kernel density curve of the Safe group presents a sharp peak and narrow band shape, with probability density highly concentrated in the low RER region, while the FO group exhibits a wide and heavy-tailed distribution, with an elongated box and high-value outliers. The violin plot displays a right-skewed and long-tailed shape, reflecting enhanced fluctuation of reconstruction errors under foreign object intrusion.

The discreteness of this error distribution can be attributed to the physical effects caused by foreign object intrusion under the coil offset state. The introduction of metal foreign objects not only alters the electromagnetic field distribution but may also lead to physical displacement of the receiving coil, thereby triggering complex changes in signal characteristics, including harmonic distortion, phase shift, and amplitude fluctuation. As shown in Fig. 11, (a)–(d) demonstrate the impact of four different test metal foreign objects on the inverter's output voltage and current at an 85 kHz frequency. The yellow waveform represents the inverter output voltage, while the white and pink waveforms show the inverter output current before and after foreign object intrusion. The influence of these metal foreign objects on electrical parameters is difficult to detect

with the naked eye. While Fig. 11(e) demonstrates the system's real-time response performance, presenting the transient waveforms during the intrusion of a can. When the calculated change in RER exceeds the safety threshold, the status flag is set high. It can be observed that there is an approximate 26 ms delay between the object intrusion and the rising edge of the decision flag. After the flag is triggered, the system activates the protection mechanism to limit the charging current output.

However, the multi-parameter fusion features extracted by this method still exhibit significant deviations, enabling the dictionary learning model to successfully complete fault classification even in the absence of obvious waveform distortion. Furthermore, these factors collectively increase the diversity of the feature space, making it more challenging for the foreign object dictionary to reconstruct such signals, which manifests as dispersion of RER values and high-value outliers. Specifically, coil offset disrupts the symmetry and stability of the signal, reducing the consistency of sparse coding and thereby broadening the distribution range of reconstruction errors. Nevertheless, using the reconstruction error ratio as a classification decision criterion performs effectively, indicating that RER can reliably distinguish between the safe state and the foreign object intrusion state.

D. Feature Ablation Analysis

To address the trade-off between detection performance and sensing complexity, and to quantify the contribution of different feature categories to the model's accuracy, a feature ablation study was conducted. The 14-dimensional feature set was divided into three progressive configurations based on hardware accessibility and computational depth:

Group I: Includes only the basic input/output parameters available in standard feedback control loops (f, R_L, $V_{bus,i}$, $I_{bus,i}$, $I_{output,i}$, $V_{output,i}$).

Group II: Adds the high-frequency AC parameters from the compensation network (φ_i, $I_{coil\_RMS,i}$, $V_{Lfl\_RMS,i}$, $V_{Cfl\_RMS,i}$, $V_{Cp\_RMS,i}$). The current is sampled through a current transformer, and the voltages are sampled through isolation amplifiers.

Group III (Proposed: full set with engineered features): Adds the derived physics-based features ($\Delta\varphi_i$, R_{cap}, I_{bus_norm}) designed to decouple load variations from foreign object disturbances.

The detection performance for each group was evaluated using the same test set. The results are summarized in Fig. 12. Using only Group I features results in a relatively low recall rate (86.20%). High-power wireless charging systems naturally exhibit fluctuations in DC bus currents due to efficiency variations. Small foreign objects cause power losses that are often indistinguishable from these natural fluctuations, leading to missed detections. The addition of Group II features significantly boosts Recall to 93.50%. This confirms that the impedance changes caused by the eddy current effect are most directly observable within the resonant tank, making these sensors critical for sensitivity.

While Group II improves sensitivity, the FAR remains at

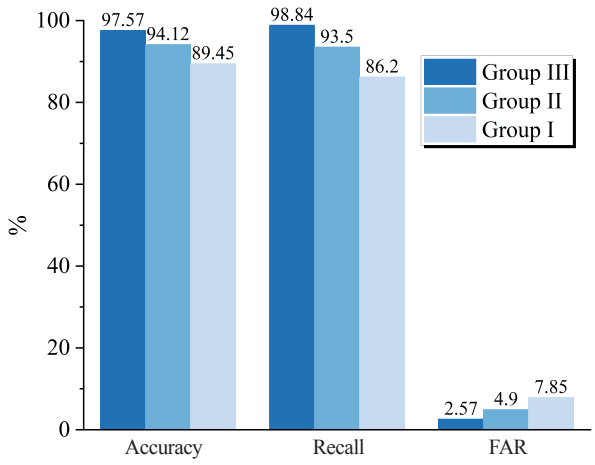

Fig. 12. Bar chart of feature ablation experiment results.

4.90%, primarily due to misjudgments during load changes or coil misalignments which also alter resonant voltages. The introduction of Group III (the proposed derived features) reduces the FAR to 2.57% while maximizing Recall. Specifically, the I_{bus_norm} and $\Delta\varphi_i$ mathematically remove the baseline trend caused by load changes. As observed in the feature weight analysis in Fig. 8(d), these engineered features are assigned high sparse coding weights, validating that they are essential for distinguishing between normal state change and foreign object intrusion.

VI. Conclusion

A hybrid detection method based on multi-parameter information fusion and transfer dictionary learning to address the challenges of foreign object detection in inductive coupled power transfer systems was proposed. Through system modeling, algorithm design, experimental verification, and platform testing, the effectiveness, robustness, and practicality of the proposed method are comprehensively evaluated. The main contributions of this paper include: although dictionary learning and transfer learning are commonly applied in fault diagnosis, this is the first attempt to combine unsupervised sparse coding with incremental learning for foreign object detection in ICPT systems. By leveraging the collaborative operation of dual dictionaries, safe states and foreign object states are effectively distinguished, overcoming the issue of insufficient generalization of traditional methods toward unknown metals. Additionally, a decision mechanism centered on the reconstruction error ratio is developed to simplify the classification process. TABLE IV presents a performance comparison between this study and some existing FOD research. Compared to methods using detection coils, this approach also maintains an accuracy advantage. Compared with other neural network models, dynamically expanding the atoms of the foreign object dictionary via the transfer learning component enables small-sample model updates, which improves detection accuracy, reduces

TABLE IV
COMPARISON BETWEEN THE EXISTING FOD METHODS AND THE DETECTION METHOD PROPOSED IN THIS ARTICLE

Reference	Method	FOD principle	Performance
[12]	With sensor	Voltage variation of sensing coil	2.7 V sensing voltage, 0.2 V blind spot FOD voltage threshold
[13]	With sensor	Voltage and frequency variation of sensing coil	5.5% and 30 kHz (Iron sheet of 30*30 mm^2)
[15]	With sensor	Voltage variation of sensing coil	94.75% overall accuracy(68.25% in conventional FOD method)
[20]	Sensorless	Normal neural network	Over 80% accuracy
[21]	Sensorless	A multilayer neural network with multivalued neurons	80.27% classification rate
[25]	With sensor	Voltage variation of Multi-thread sensing coil	68% increased
[26]	Sensorless	Resonance Frequency Deviation	200 ms detection speed and 49% detection area with beverage cans and coins
[27]	Sensorless	Total Harmonic Distortion (THD) of input current	Disk-shaped coins (5.65% in normal and 5.11% in invade)
[28]	With sensor	Voltage variation of LC resonant circuit	97.56% sensitivity (92.89% sensitivity for coin in a 3.3 kW system)
[29]	With sensor	Voltage variation of sensing coil	162 mV sensing voltage for coin and 50 mV for bolt (300 W system)
[30]	Sensorless	Voltage variation of sensing coil	0.1 V threshold voltage (40*40 mm^2 metal object)
this work	Sensorless	Dictionary and Transfer Learning	97.51% accuracy (watch under 40*40 mm^2)

computational costs, and thus holds practical application value. Future work based on this research should focus on exploring more efficient sparse coding algorithms, further reducing computational complexity, and enhancing detection precision.

REFERENCES

[1] Z. Li, W. Zhang, Z. Gan, and B. Li, "Study on composite structure of tian-font magnetic shielding and anti-series active coils for wireless power transfer system," in *CPSS Transactions on Power Electronics and Applications*, vol. 10, no. 1, pp. 97–109, Mar. 2025.

[2] G. Yang, J. Su, A. Ali, Z. Tong, J. Zhang, X. Qu, and F. Blaabjerg, "Analysis and design of a dual-coupled LCC-S compensated IPT system considering air gap variation," in *IEEE Transactions on Transportation Electrification*, vol. 11, no. 5, pp. 11714–11727, Oct. 2025.

[3] X. Lv, X. Dai, F. Yu, X. Li, H. Wang, Y. Sun, and J. Hu, "A high misalignment tolerance SCC-WPT system with relay single capacitive coupler for UAV wireless charging applications," in *IEEE Transactions on Power Electronics*, vol. 40, no. 8, pp. 10372–10377, Aug. 2025.

[4] I. Martínez De Alegría, I. Rozas Holgado, E. Ibarra, E. Robles, and J. L. Martín, "Wireless power transfer for unmanned underwater vehicles: Technologies, challenges and applications," in *Energies*, vol. 17, no. 10, p. 2305, May 2024.

[5] L. Wang, P. Sun, Y. Liang, L. He, X. Wu, and Q. Deng, "Research on the control strategy of communication-free IPT system based on multiparameter joint real-time identification," in *IEEE Transactions on Power Electronics*, vol. 39, no. 1, pp. 1912–1926, Jan. 2024.

[6] S. Li, W. Li, J. Deng, T. D. Nguyen, and C. C. Mi, "A double-sided LCC compensation network and its tuning method for wireless power transfer," in *IEEE Transactions on Vehicular Technology*, vol. 64, no. 6, pp. 2261–2273, Jun. 2015.

[7] Z. Li, Z. Chen, M. Yang, Y. Cheng, X. Xiong, and S. Huang, "Design of edge-enhanced coil structure to obtain constant mutual inductance with horizontal misalignment in wireless power transfer systems of electric vehicles," in *CPSS Transactions on Power Electronics and Applications*, vol. 9, no. 2, pp. 141–151, Jun. 2024.

[8] Z. Huang, B. Zou, Z. Huang, H. H. -C. Iu, and C. K. Tse, "A single-stage IPT converter with optimal efficiency tracking and constant voltage output against dynamic variations of coupling and Load," in *IEEE Transactions on Transportation Electrification*, vol. 11, no. 1, pp. 1582–1592, Feb. 2025.

[9] J. Xia, S. Li, T. Li, W. Dai, Z. Liu, and S. Lu, "An efficiency optimization method for doubled-sided LCC compensated inductive power transfer systems based on circuit parameter matching," in *IEEE Transactions on Power Electronics*, vol. 40, no. 4, pp. 6260–6271, Apr. 2025.

[10] B. Zhang, Z. Zhu, and Z. Xi, "Sensitivity optimization method for metal object Detection in electric vehicle wireless charging system," in *Journal of Power Supply*, vol. 22, no. 4, pp. 209–218, Aug. 2024.

[11] L. Li, L. Yang, C. Cai, F. Zhang, X. Wang, and H. Chen, "An active metal object detection scheme for wireless power transfer system based on impedance variation," in *Electrical Measurement & Instrumentation*, vol. 59, no. 5, pp. 172–179, 2022.

[12] Z. Yang, C. Xia, S. Zhao, H. Li, Y. Peng, L. Xiang, and W. Li, "Non-blind zone MOD method based on incomplete compensation of detection coil for electric vehicle eireless charging system," in *Proceedings of the CSEE*, vol. 42, no. 20, pp. 7363–7375, Oct. 2022.

[13] Z. Yang, C. Xia, A. Sun, X. Wang, S. Zhao, and F. Li, "Dual-mode foreign object detection system for mtal and live object detection in wireless electric vehicle charger," in *IEEE Transactions on Power Electronics*, vol. 40, no. 9, pp. 11923–11927, Sept. 2025.

[14] Y. Wang and N. Xia, "A design of three-stage location and detection system for the metallic foreign body applied in the wireless power transfer system," in *Journal of Electric Power Science and Technology*, vol. 37, no. 2, pp. 205–212, 2022.

[15] S. Niu, C. Zhang, Y. Shi, S. Niu, and L. Jian, "Foreign object detection considering misalignment effect for wireless EV charging system," in *ISA Transactions*, vol. 130, pp. 655–666, Nov. 2022.

[16] Y. Sun, T. Zhou, K. Song, C. Zhu, and G. Wei, "Design of high-order composite resonant topology for improving the sensitivity of foreign object detection system," in *Transactions of China Electrotechnical Society*, vol. 38, no. 6, pp. 1541–1552, Mar. 2023.

[17] S. Zhao, C. Xia, C. Lu, Z. Yang, and A. Sun, "Identification of metal object types by high and low frequencies detection for wireless EV charger," in *IEEE Transactions on Power Electronics*, vol. 40, no. 1, pp. 2581–2592, Jan. 2025.

[18] T. Wu, X. Yang, H. Zhu, Y. Wu, L. Yang, and D. Zhang, "Feature sequence fusion faster R-CNN-based metal foreign object detection for electric vehicle wireless power transfer system," in *2023 IEEE 7th Conference on Energy Internet and Energy System Integration (EI2)*, Hangzhou, China, 2023, pp. 3713–3719.

[19] N. Rajamanickam, D. S. Abraham, R. Alroobaea, and W. M. Abdelfattah, "Foreign object debris detection on wireless electric vehicle charging pad using machine learning approach," in *Processes*, vol. 12, no. 8, pp. 1574,

Jul. 2024.
[20] Y. Gong, Y. Otomo, and H. Igarashi, "Sensorless metal object detection for wireless power transfer using machine learning," in *COMPEL - International Journal Computation Mathematics Electronic Engineering*, vol. 41, no. 3, pp. 807–823, May 2022.
[21] M. Bindi, V. S. Meshram, A. Luchetta, L. Becchi, M. Intravaia, A. Trivino, and E. Villagrasa, "Foreign object detection for wireless power transfer systems using MLMVN," in *2024 IEEE 8th Forum on Research and Technologies for Society and Industry Innovation (RTSI)*, Milano, Italy, 2024, pp. 453–458.
[22] M. Dhaini, M. Berar, P. Honeine, and A. Van Exem, "Unsupervised domain adaptation for regression using dictionary learning," in *Knowledge-Based Systems*, vol. 267, p. 110439, May 2023.
[23] N. Pan, Y. Li, and J. Chen, "Research on ultrasonic flowmeter echo signal processing based on K-SVD dictionary learning," in *Journal of Electronic Measurement and Instrumentation*, vol. 39, no. 1, pp. 195–202, 2025.
[24] M. Li, Y. Li, and Z. Li, "A comprehensive survey of transfer dictionary learning," in *Neurocomputing*, vol. 623, p. 129322, Mar. 2025.
[25] Y. Tian, Y. Lin, J. Tian, and L. Xiang, "Multi-thread sensing coil design for metal object detection of wireless power transfer systems," in *Measurement*, vol. 184, p. 109952, Nov. 2021.
[26] M. Moghaddami and A. I. Sarwat, "A sensorless conductive foreign object detection for inductive electric vehicle charging systems based on resonance frequency deviation," in *2018 IEEE Industry Applications Society Annual Meeting (IAS)*, Portland, OR, USA, 2018, pp. 1–6.
[27] P. Maile and S. Jayalth, "Foreign object detection using total harmonic distortion of input current," in *2025 IEEE Wireless Power Technology Conference and Expo (WPTCE)*, Rome, Italy, 2025, pp. 1–5.
[28] Y. Sun, T. Zhou, J. Jiang, G. Wei, C. Zhu, and K. Song, "High-sensitivity detection method for metal foreign objects based on frequency optimization in wireless electric vehicles charging," in *Energies*, vol. 16, no. 2, p. 741, Jan. 2023.
[29] W. Zhong, F. Xiang, and C. Hu, "Metal object detection with detection coils perpendicular to power coils for wireless power transfer systems," in *IEEE Transactions on Power Electronics*, vol. 38, no. 9, pp. 10530–10534, Sept. 2023.
[30] V. X. Thai, G. C. Jang, S. Y. Jeong, J. H. Park, Y. -S. Kim, and C. T. Rim, "Symmetric sensing coil design for the blind-zone free metal object detection of a stationary wireless electric vehicles charger," in *IEEE Transactions on Power Electronics*, vol. 35, no. 4, pp. 3466–3477, Apr. 2020.

Zhan'anxin Tong was born in China in 1996. He received the B.E. degree in Electrical Engineering in 2018 from Chongqing University, Chongqing, China, and the M.E. degree in Control Engineering in 2022 from the Hefei University of Technology, Hefei, China, where he is currently working toward the Ph.D. degree in electrical engineering.

His current research interests include wireless power transfer and machine learning.

Jianhui Su received the B.S., M.S., and Ph.D. degrees in Electrical Engineering from Hefei University of Technology, Hefei, China, in 1984, 1987, and 2003, respectively. He is currently a Professor with the School of Electrical Engineering and Automation, Hefei University of Technology, and also the Associate Director of the Research Center for Photovoltaic System Engineering, Ministry of Education, Hefei.

His current research interests include renewable power generation, special power supplies, distributed power generation systems, and high-voltage transducer control technologies.

Shiyu Wang received B.S. degree in Automation in Northeast Electric Power University, Jilin, China, in 2020, and the M.S. degree in Sustainable Energy in the University of Glasgow, Scotland, in 2021. Now she is currently pursuing the Ph.D. degree in energy and power (electrical engineering) in Hefei University of Technology, Hefei, China. Her current research interests include the estimation of state of Lithium-ion batteries and energy management in micro-grid.

Yan Du received the B.Sc. degree in Automatic Engineering and the M.Sc. and Ph.D. degrees in Power Electronics and Power Drives from Hefei University of Technology, Hefei, China, in 2000, 2004, and 2013, respectively.

She is currently an Associate Professor with the School of Electrical Engineering and Automation, Hefei University of Technology. Her current research interests include distributed generation and microgrid (MG) control.

Meiqin Mao received the B.Sc., M.Sc., and Ph.D. degrees in Electrical Engineering from Hefei University of Technology in 1983, 1988, and 2004 respectively. She is now a Professor with School of Electrical and Automation Engineering, Hefei University of Technology, China. Her research interests include renewable energy generation technology, distributed power generation and microgrids, power electronics applied in power system. She has published more than 200 journal/conference technical papers.